Supporting Information: Imaging strain-controlled magnetic reversal in thin CrSBr

Kousik Bagani[1†], Andriani Vervelaki[1†], Daniel Jetter[1], Aravind Devarakonda[2,3], Märta A. Tschudin[1], Boris Gross[1], Daniel G. Chica[4], David A. Broadway[1,5], Cory R. Dean[3], Xavier Roy[4], Patrick Maletinsky[1], Martino Poggio[1,6*]

[1]Department of Physics, University of Basel, 4056 Basel, Switzerland.
[2]Department of Physics, Columbia University, New York, NY 10027, USA.
[3]Department of Applied Physics and Applied Mathematics, Columbia University, New York, NY 10027, USA.
[4]Department of Chemistry, Columbia University, New York, NY 10027, USA.
[5]School of Science, RMIT University, Melbourne 3001, Australia.
[6]Swiss Nanoscience Institute, University of Basel, 4056 Basel, Switzerland.

*Corresponding author(s). E-mail(s): martino.poggio@unibas.ch;
†These authors contributed equally to this work.

1 Methods

1.1 CrSBr ribbons

CrSBr single crystals are grown using the chemical vapor transport technique as described in Scheie et al. [1]. Nominally unstrained CrSBr ribbons are obtained by mechanical exfoliation of bulk crystals onto SiO_2/Si chips. A polycarbonate/polydimethylsiloxane (PC-PDMS) transfer stamp [2] is used to pick up exfoliated hBN, CrSBr, and a metallized graphite micro-manipulator in sequence. See Kapfer et al. [3] for micro-manipulator preparation. Subsequently, the completed stack is flipped onto a target SiO_2/Si chip such that the CrSBr flake and micro-manipulator are exposed. The micro-manipulator is maneuvered to deform the CrSBr flake using an AFM operated in contact mode and the "Nanoman" software (Bruker).

We measure the thickness of different regions of the sample using AFM. We convert this measurement to a number of atomic layers using a thickness of 0.78 nm/layer for all layers [4, 5] except the first layer, which is in direct contact with the hexagonal boron nitride and is assumed to be 1.1-nm-thick based on the measurement.

1.2 Map of inhomogeneous strain

To calculate the inhomogeneous strain produced in the bent CrSBr ribbon, we use a coordinate system aligned with the ribbon's crystallographic axes before bending, as shown in Figure 1b. In this system, the a- and b-axis represent the original crystallographic directions and x_a and x_b denote positions along these directions. We obtain a map of the strain from $\varepsilon(x_a, x_b) = -l(x_a, x_b)/\rho(x_a)$, where $l(x_a, x_b)$ is the perpendicular distance from the neutral axis, $\rho(x_a) = (1 + (\frac{d\delta(x_a)}{dx_a})^2)^{3/2} / \frac{d^2\delta(x_a)}{dx_a^2}$ is the local radius of curvature, and $\delta(x_a)$ is the deflection of the ribbon at a given position along the neutral axis [3]. We determine $\delta(x_a)$ by fitting the ribbon's topographic outline with a 4th-order polynomial. We then calculate a map of $\varepsilon(x_a, x_b)$, shown in Figure 1d, quantifying the variation of a-axis strain in the sample plane.

On the two long edges of the ribbon, the tensile and compressive strain reach a maximum of 0.25%. A tiny segment of ribbon near the fracture experiences the most bending, resulting in a maximum strain of approximately 1.5%. Note that according to Cenker et al., the maximum tensile strain of this region should be sufficient to force the magnetization into a F configuration in remanence [6]. As seen in Figure 1 of the main text, this region remains in the AF configuration in remanence along with the rest of the ribbon. This behavior may be because the threshold value for the tensile strain reported by Cenker et al. does not precisely apply to our experimental situation: the temperature in our case is 4.2 K, while in Cenker et al. it is 15 K. Second, the narrow width of this region puts the tensile and compressive regions in very close proximity. This confined area and the large strain gradient therein may prevent the transition to the F state.

1.3 SQUID-on-lever

We fabricate the SQUID-on-lever scanning probes by sputtering Nb on a AFM cantilever and patterning its apex via focused-ion-beam milling, as described by Wyss et al. [7]. Each hybrid AFM/SQUID sensor is characterized and operated at 4.2 K in a semi-voltage biased circuit, in which the current response I_{SQUID} is measured by a

series SQUID array amplifier (Magnicon). Two different SQUID-on-lever sensors were used for this study. Their effective diameters of 175 nm and 185 nm are extracted from their corresponding quantum interference patterns. The sensors have an AC magnetic field sensitivity exceeding $S_B^{1/2} = 1\ \mu T\ \mathrm{Hz}^{-1/2}$ in the white-noise regime.

1.4 Magnetic imaging

Magnetic imaging is carried out in a custom-built scanning probe microscope operating under high vacuum within a ^{4}He cryostat. The SQUID-on-lever scanning probe is capable of simultaneously performing non-contact AFM and scanning SQUID microscopy. The cantilever is excited to an amplitude of $\Delta z = 16$ nm at its fundamental mechanical resonance frequency of $f_0 \simeq$300 kHz by a piezo-electric actuator driven by a phase-locked loop. Displacement oscillations are detected using a fiber-optic interferometer. A lock-in amplifier is used to demodulate the B_z^{ac} signal. Since I_{SQUID} is proportional to magnetic flux, this response provides a measure of the local magnetic field threading through the SQUID loop. Note that the axis of the SQUID is tilted by 10° with respect to the z-axis, because the SQUID-on-lever is scanned in a standard AFM configuration designed to easily approach the sensor tip without touching the rest of the cantilever body. As a result, both $B_z(x, y)$ and $B_z^{\mathrm{ac}}(x, y)$ are measured with a 10° tilt with respect to the z-axis. Simulated maps of the same quantities take this tilt into account. The pixel size of the magnetic images varies from 35 to 65 nm and the acquisition time is around 0.2 s/pixel. The time constant used for the B_z^{ac} scans is $\tau \simeq 150$ ms. We measure the response of I_{SQUID} as a function of the out-of-plane applied magnetic field $\mu_0 H_z$ before and after each scan for a field range larger than that produced by the ribbon. By scanning the sample using a scanning probe controller (Specs) and piezoelectric actuators (Attocube) at a constant tip-sample spacing of 250 nm, we map $B_z(x, y)$ and $B_z^{\mathrm{ac}}(x, y)$ in a plane above the sample. $B_z^{\mathrm{ac}} \propto dB_z/dz$ is measured by demodulating the SQUID-on-lever response at the cantilever oscillation frequency. Due to spectral filtering, the resulting signal contains less noise than DC measurements of B_z. Spatial resolution is limited by the tip-sample spacing and by the ∼180 nm effective diameter of the SQUID loop.

In all imaging experiments, we apply a small out-of-plane field between $\mu_0|H_z| = 10$ and 20 mT. This out-of-plane field ensures that the SQUID sensor, whose magnetic sensitivity is field-dependent, is sensitive enough to measure the sample's stray fields. Each layer's strong in-plane anisotropy should ensure that the magnetization remains nearly unaffected by the small H_z [8].

1.5 Micromagnetic simulations

We simulate the magnetization configuration of the CrSBr ribbons using the *Mumax*^{3} software package [9–11], which uses the Landau-Lifshitz-Gilbert micromagnetic formalism with finite-difference discretization. To mimic the layered structure of CrSBr, we set the thickness of a cell in the finite-difference mesh to the thickness of a CrSBr layer. We use literature values to set the saturation magnetization $M_{\mathrm{sat}} = 36\,\mu_{\mathrm{B}}/\mathrm{nm}^2$ [12, 13], the magnetocrystalline anisotropy along the a- and b-axis $K_{\mathrm{u,a}}$, $K_{\mathrm{u,b}}$ [12], and the intralayer exchange interactions J_1, J_2, J_3 [1]. These exchange interactions are used to estimate the intralayer exchange stiffness $A_{\mathrm{ex,\ intra}}$ [14]. We estimate the interlayer exchange stiffness $A_{\mathrm{ex,\ inter}}$ and its dependence on strain from theoretical calculations [15].

For the values of strain considered in this study, $A_{\text{ex, inter}}$ depends linearly on strain. As a starting point, we simulate the magnetic hysteresis of a cube of 200 nm$\times$200 nm$\times$200 nm using a cell size of 4 nm$\times$4 nm$\times$0.8 nm and periodic boundary conditions. We compare the results to bulk hysteresis measurements [5, 13, 16] along the a- b- and c-axis and modify the values to $K_{\text{u, a}} = 72$ kJ/m^3, $K_{\text{u, b}} = 127$ kJ/m^3, and $A_{\text{ex, inter}} = -23$ fJ/m in order to optimize the match. Changes in $A_{\text{ex, intra}}$ do not have a significant influence on the simulated hysteresis (within $1-10$ pJ/m range). Therefore, we choose $A_{\text{ex, intra}} = 8$ pJ/m to increase the exchange length l_{ex}, allowing us to simulate a larger area.

For the simulation of the strained ribbon, the geometry and thickness in number of layers is determined from AFM measurements. The simulations assume a uniform thickness of 18 layers, ignoring the narrow region along the right edge of the ribbon consisting of a single-layer strip followed by a step with decreased thickness (14 layers). The structure is discretized into cells of size 8 nm $\times$ 8 nm $\times$ 0.8 nm. Starting from the value of $A_{\text{ex, inter}}$ determined for the simulation of bulk material and its theoretical strain dependence, we adjust this dependence to optimally reproduce both the measured magnetic hysteresis and the measured stray field patterns, resulting in $A_{\text{ex, inter}} = (16.3\varepsilon(\%) - 23)$ fJ/m, where ε is the strain along the a-axis. This linear dependence agrees roughly with previous observations, predicting an AF to F transition at 1.5% strain compared to the observed 1.3% [6]. The spatial variation of strain is implemented by dividing the ribbon into 110 regions of uniform $A_{\text{ex, inter}}$, corresponding to the average value in that region.

Simulated $B_z(x, y)$ and $B_z^{\text{ac}}(x, y)$ are calculated from the magnetization maps generated by *Mumax*^{3} at a height of 250 nm above the sample, corresponding to our SQUID-sample distance. $B_z^{\text{ac}}(x, y)$ is calculated assuming $\mathrm{d}z = 16\,\text{nm}$, which corresponds to the oscillation amplitude of the cantilever. Finally, we apply a Gaussian blurring of $2\sigma = 192\,\text{nm}$ to approximate the point-spread function of the SQUID sensor.

2 Additional measurements and simulations

2.1 Topographic imaging

Supporting Figure 1a is an AFM image of the strained ribbon. Supporting Figures 1b-d show that the width of the narrow single-layer strip running along the right edge of the ribbon and 14-layer-thick region immediately to its right remain undisturbed along the entire length of the flake, even past the crack shown in Supporting Figure 1d.

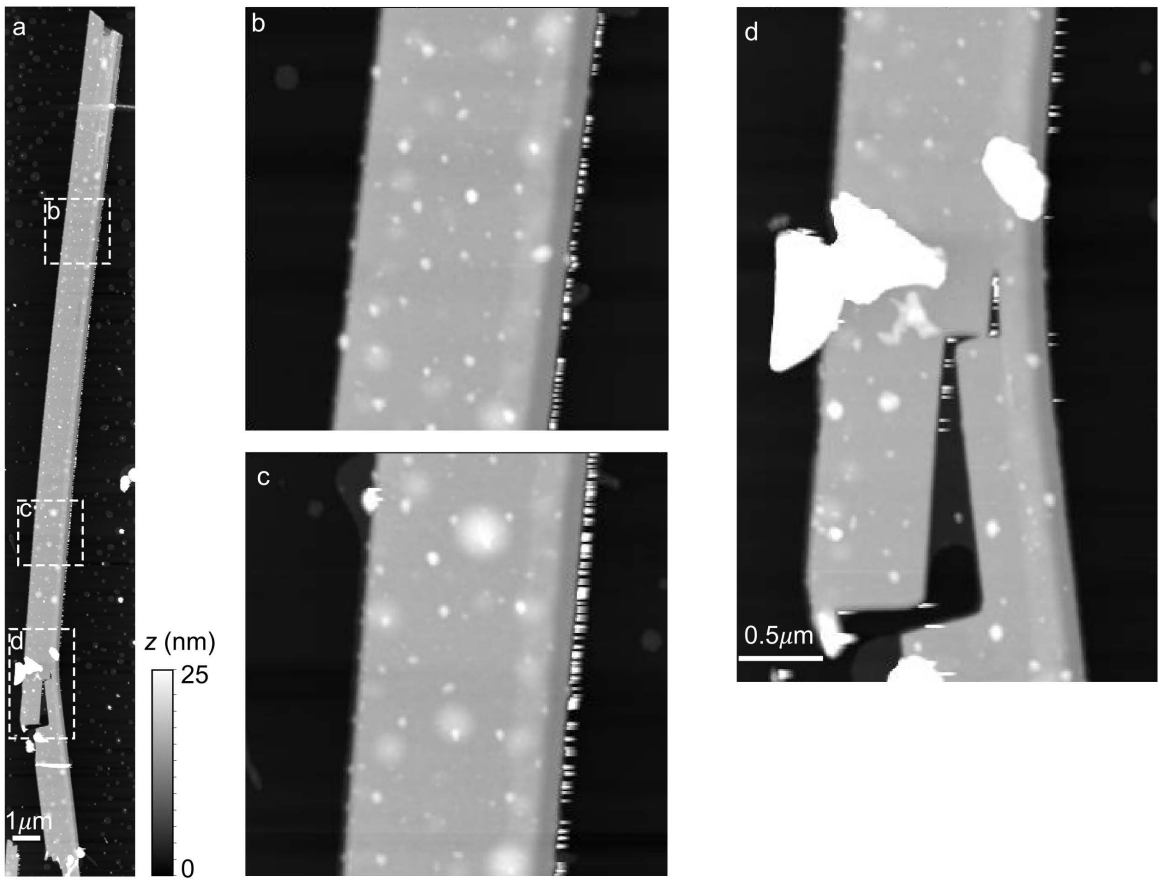

Supp. Fig. 1 AFM images of the strained ribbon. (a) A topographic image of the strained ribbon . (b)-(d) Zoom-in images for the regions indicated by the white dashed boxes in (a).

2.2 Magnetic imaging

We image the local magnetic response of the CrSBr ribbons to a changing field H_x, applied nearly along the b-axis. To help visualize the layer-by-layer changes in magnetization, we replot the data shown in Figure 2 of the main text with schematic diagrams corresponding to the magnetization configurations of the ribbons at different applied fields. Supporting Figures 2b and d show the configurations for cross-sections indicated by black dashed lines in Supporting Figures 2a and c, respectively. It is worth mentioning that we do not know the

exact order in which the interior layers reverse, only that the outer layers reverse first, followed by the interior layers at much higher fields.

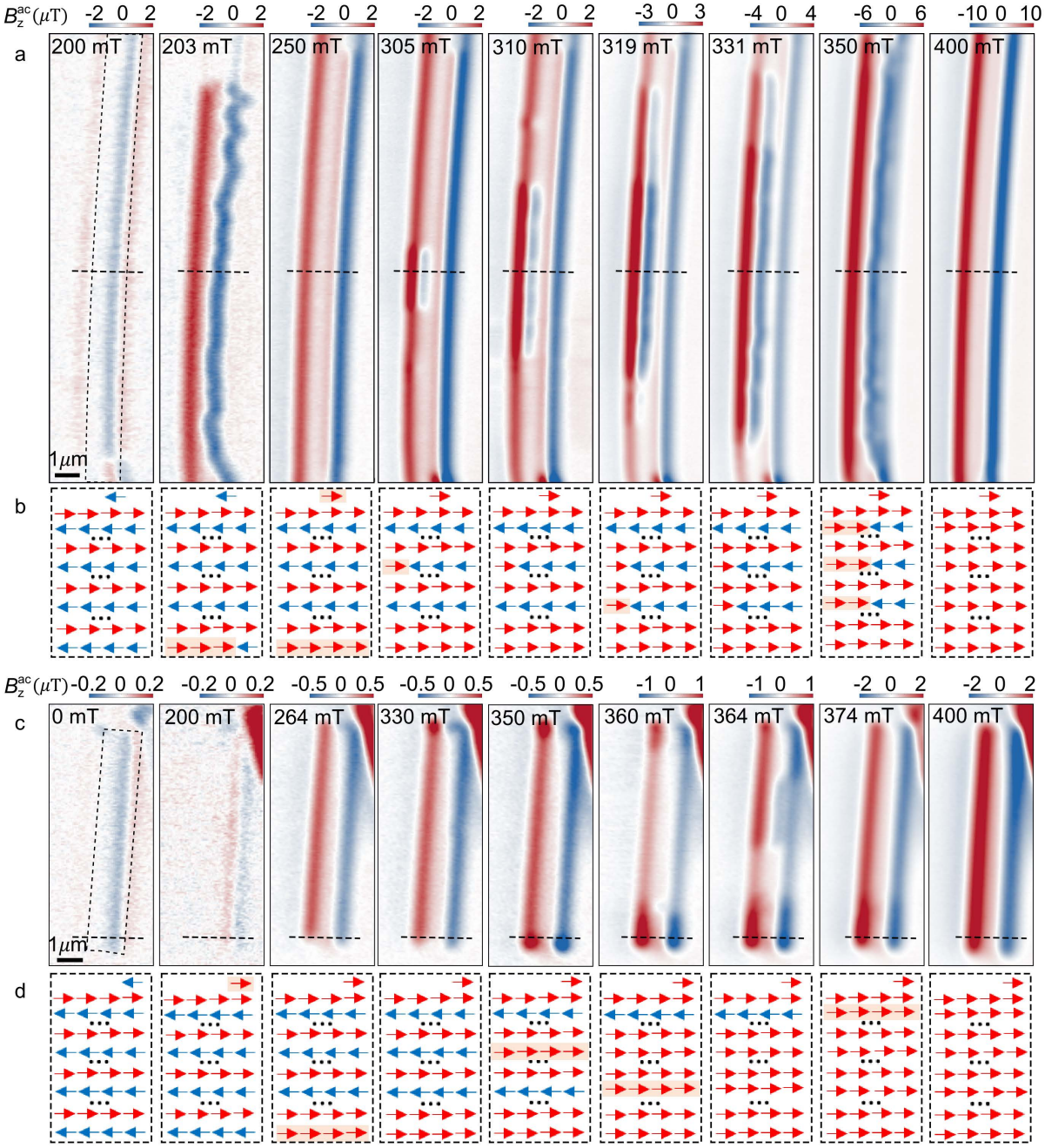

Supp. Fig. 2 Magnetic field evolution and spin configuration of strained and pristine ribbons. (a) $B_z^{ac}(x, y)$ maps of the strained ribbon under a progressively increasing magnetic field H_x. (b) Schematic illustration of the spin configuration along the cross-sections marked by black dashed lines in (a). The layers undergoing reorientation are highlighted in yellow. (c) $B_z^{ac}(x, y)$ images of the pristine ribbon and (d) schematic illustrations of the corresponding spin configuration.

In addition to the measurements shown in Figure 2 of the main text, Supporting Figures 3 and 4 show magnetic images of the strained ribbon measured as H_x is swept both upwards and downwards. Similarly, Supporting Figures 5 and 6 show images of the pristine ribbon as H_x is swept both upwards and downwards. We saturate both ribbons at $\mu_0 H_x = -500$ mT before sweeping the field to zero and starting the upward measurement. Before the downward measurement, the ribbons were fully polarized in an applied field $\mu_0 H_x = 600$ mT. In all cases, we measure both B_z and $B_z^{\mathrm{ac}} \propto dB_z/dz$, however, we only plot $B_z^{\mathrm{ac}}(x, y)$ maps, because they are more sensitive to small spatial features compared to $B_z(x, y)$.

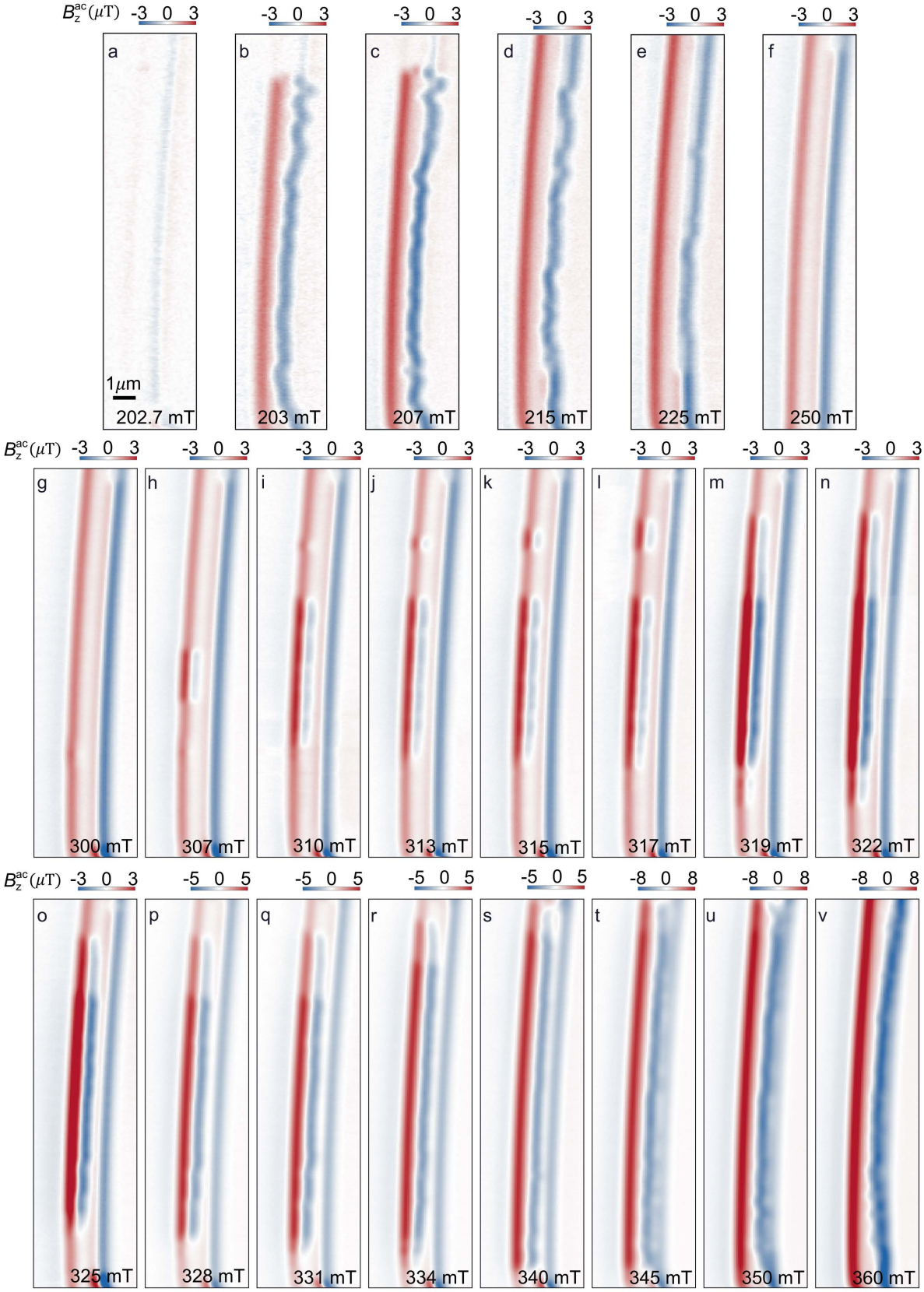

Supp. Fig. 3 Stray-field images of the strained ribbon while sweeping H_x up. $B_z^{ac}(x, y)$ with progressively increasing H_x. (a) - (f) corresponds to the reorientation of the surface layers and (g) - (v) of the interior layers.

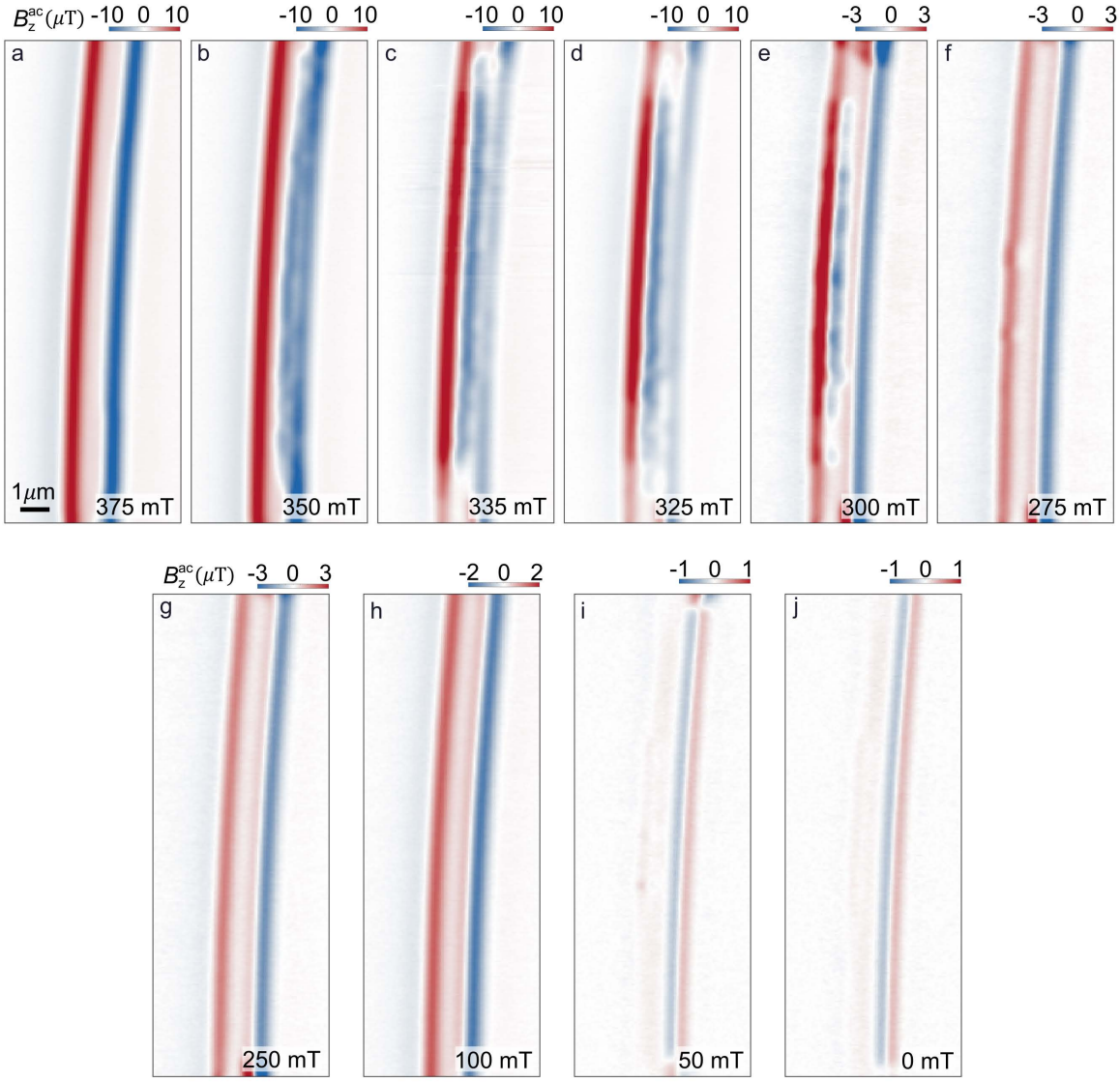

Supp. Fig. 4 Stray-field images of the strained ribbon sweeping H_x down. $B_z^{ac}(x, y)$ with progressively decreasing H_x.

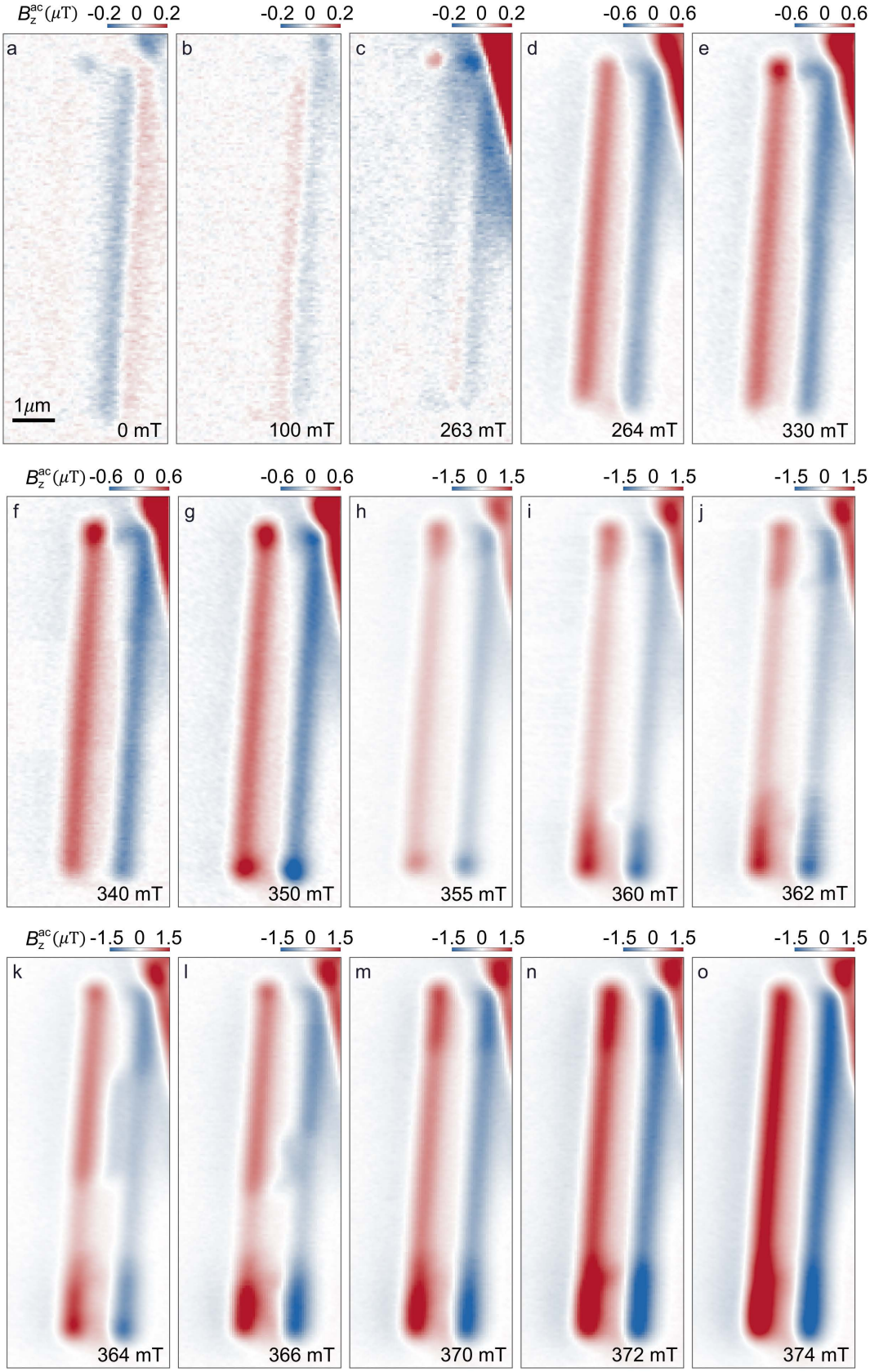

Supp. Fig. 5 Stray-field images of the pristine ribbon sweeping H_x up. $B_z^{ac}(x, y)$ with progressively increasing H_x.

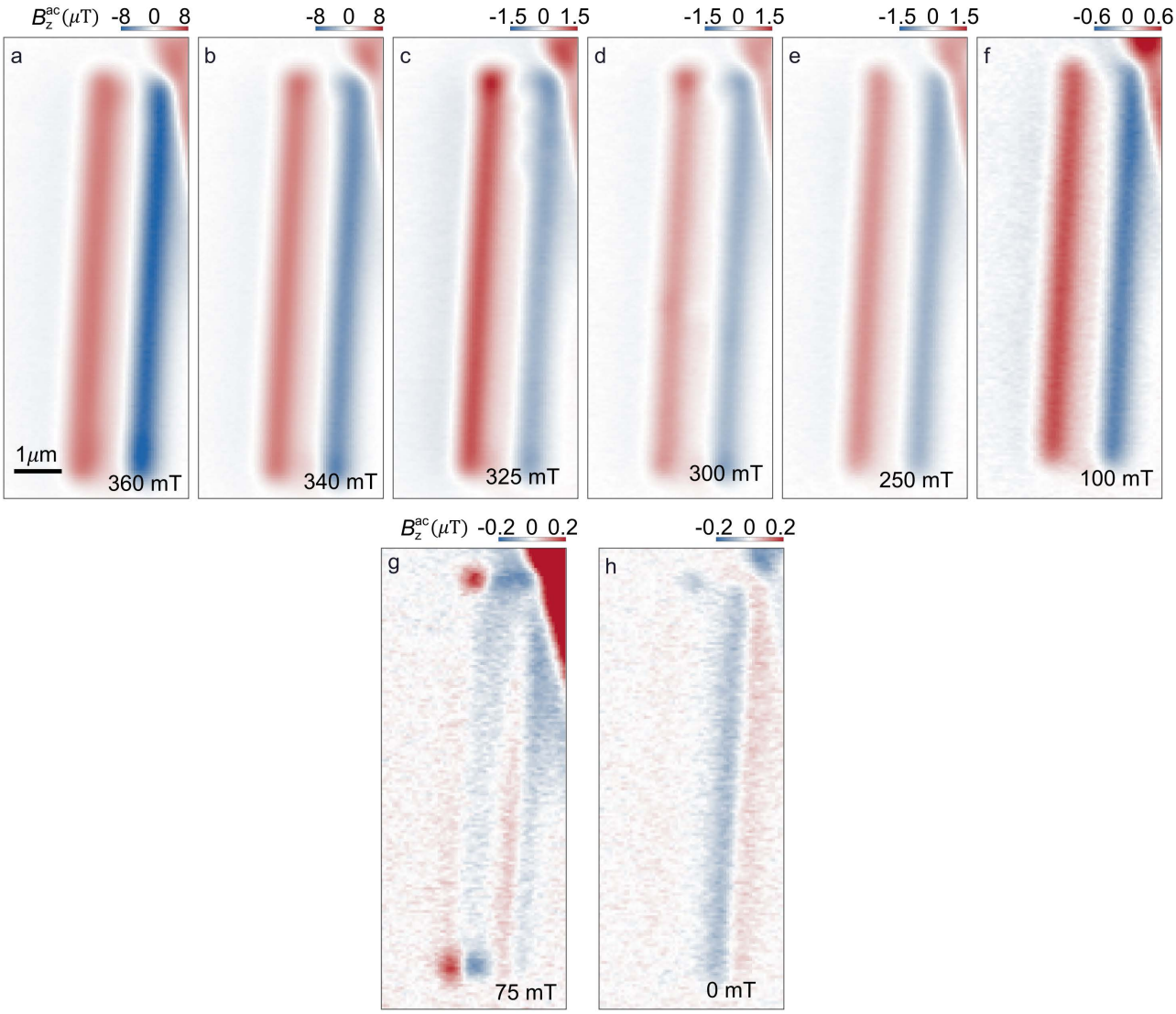

Supp. Fig. 6 Stray-field images of the pristine ribbon sweeping H_x down. $B_z^{ac}(x, y)$ with progressively decreasing H_x.

2.3 Magnetic hysteresis

A comparison between the magnetic hysteresis of the strained and pristine ribbons is shown in Supporting Figure 7, where it is evident that the pristine ribbon (red and blue dashed lines) exhibits larger hysteresis compared to the strained ribbon (orange and light blue lines). For the pristine ribbon, we average the majority of its area, excluding the top part of the ribbon to avoid the influence of the neighboring ribbon's stray field. For the strained ribbon, we use the same area selected in Figure 4a.

As discussed in the main text, we infer that the transition occurring between 200 and 300 mT on the way up corresponds to the reorientation of a single layer. This conclusion is supported by the ratio of approximately 1:9 between the step in $|B_z|_{\text{avg}}$ associated with this transition and the value of $|B_z|_{\text{avg}}$ after the ribbons reach saturation (at around 400 mT), as shown in Supporting Figure 7.

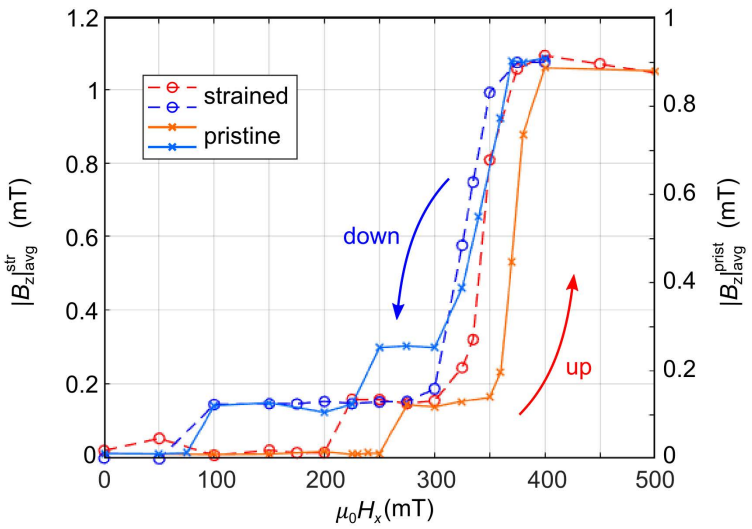

Supp. Fig. 7 Magnetic Hysteresis comparison. The vertical axes corresponds to $|B_z|$ averaged over areas of the pristine and strained ribbon and is plotted as a function of H_x. Magnetic hysteresis of the pristine flake is shown in red and blue dashed lines for the upward and downward sweeps, respectively. The hysteresis of the strained flake is shown in orange and light blue lines for the upward and downward sweeps, respectively.

2.4 Micromagnetic simulations

Micromagnetic simulations reproduce magnetic domains of the same shape and size as measured in experiment. This agreement suggests that the wavy features in the measured $B_z^{\mathrm{ac}}(x, y)$ maps do not result from unintentional inhomogeneties or defects in the sample. Rather, they are a consequence of the strain gradients induced by bending the ribbon. Supporting Figure 8 shows a comparison between measured and simulated stray-field maps showing similar features at similar values of applied H_x.

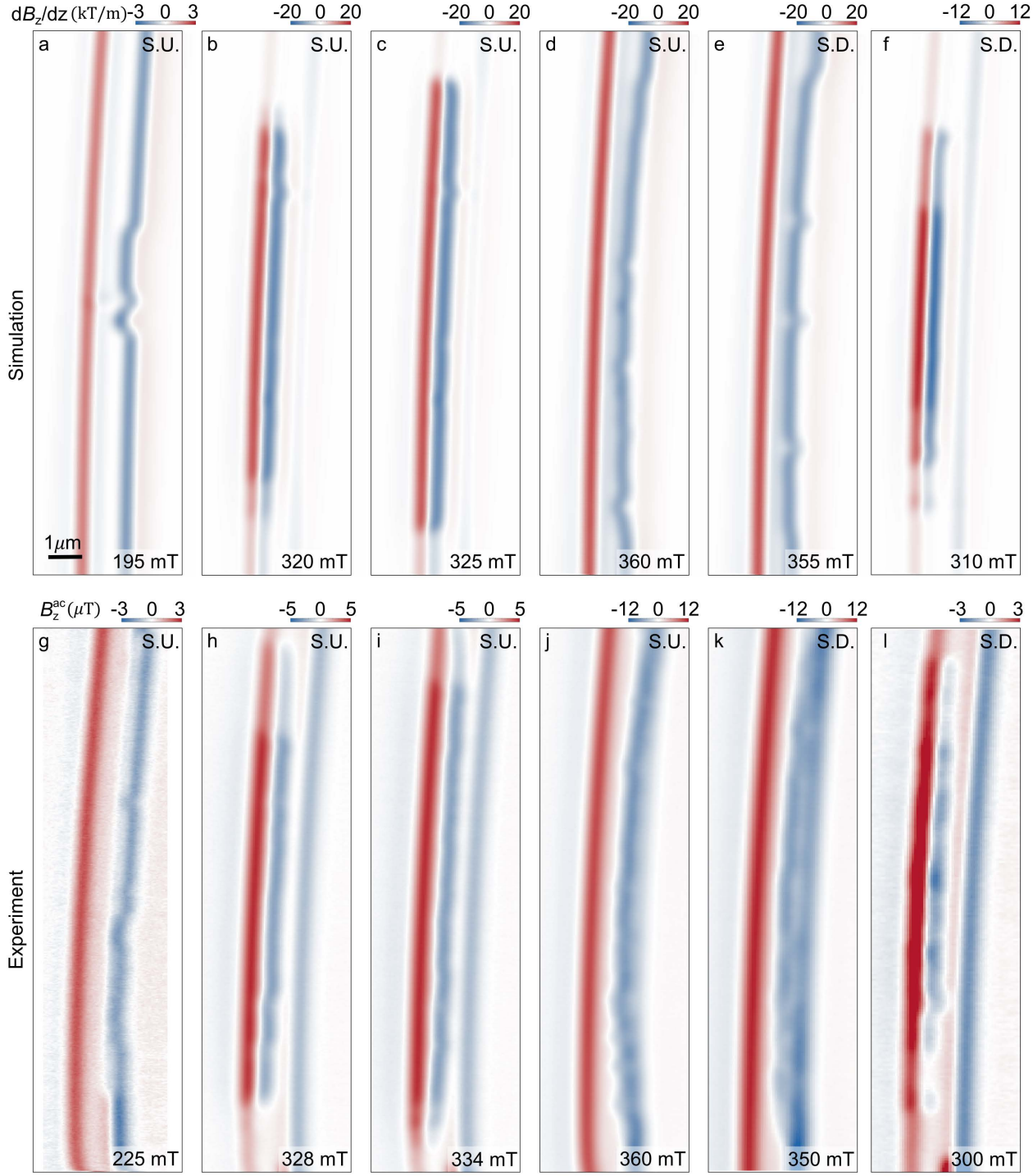

Supp. Fig. 8 Comparison between simulated and measured magnetic domains. (a) - (f) Representative simulated $\frac{\mathrm{d}B_z(x,y)}{\mathrm{d}z}$ at the applied fields H_x indicated in the bottom right of the images and (g) - (l) corresponding measurements at similar fields. Whether the maps correspond to simulations or measurements done during a sweep up (S.U.) in H_x or a sweep down (S.D.) is indicated in the top right of each image.

References

[1] Scheie, A. *et al.* Spin Waves and Magnetic Exchange Hamiltonian in CrSBr. *Advanced Science* **9**, 2202467 (2022).

[2] Wang, L. *et al.* One-Dimensional Electrical Contact to a Two-Dimensional Material. *Science* **342**, 614–617 (2013).

[3] Kapfer, M. *et al.* Programming twist angle and strain profiles in 2D materials. *Science* **381**, 677–681 (2023).

[4] Lee, K. *et al.* Magnetic Order and Symmetry in the 2D Semiconductor CrSBr. *Nano Letters* **21**, 3511–3517 (2021).

[5] Göser, O., Paul, W. & Kahle, H. Magnetic properties of CrSBr. *Journal of Magnetism and Magnetic Materials* **92**, 129–136 (1990).

[6] Cenker, J. *et al.* Reversible strain-induced magnetic phase transition in a van der Waals magnet. *Nature Nanotechnology* **17**, 256–261 (2022).

[7] Wyss, M. *et al.* Magnetic, Thermal, and Topographic Imaging with a Nanometer-Scale SQUID-On-Lever Scanning Probe. *Physical Review Applied* **17**, 034002 (2022).

[8] Telford, E. J. *et al.* Layered Antiferromagnetism Induces Large Negative Magnetoresistance in the van der Waals Semiconductor CrSBr. *Advanced Materials* **32**, 2003240 (2020).

[9] Vansteenkiste, A. *et al.* The design and verification of MuMax3. *AIP Advances* **4**, 107133 (2014).

[10] Exl, L. *et al.* LaBonte's method revisited: An effective steepest descent method for micromagnetic energy minimization. *Journal of Applied Physics* **115**, 17D118 (2014).

[11] Leliaert, J. *et al.* Adaptively time stepping the stochastic Landau-Lifshitz-Gilbert equation at nonzero temperature: Implementation and validation in MuMax3. *AIP Advances* **7**, 125010 (2017).

[12] Tschudin, M. A. *et al.* Imaging nanomagnetism and magnetic phase transitions in atomically thin CrSBr. *Nature Communications* **15**, 6005 (2024).

[13] López-Paz, S. A. *et al.* Dynamic magnetic crossover at the origin of the hidden-order in van der Waals antiferromagnet CrSBr. *Nature Communications* **13**, 4745 (2022).

[14] Skomski, R. & Coey, J. M. D. *Permanent Magnetism* (Institute of Physics Publishing, 1999).

[15] Bo, X., Li, F., Xu, X., Wan, X. & Pu, Y. Calculated magnetic exchange interactions in the van der Waals layered magnet CrSBr. *New Journal of Physics* **25**, 013026 (2023).

[16] Pei, F. *et al.* Surface-Sensitive Detection of Magnetic Phase Transition in Van Der Waals Magnet CrSBr. *Advanced Functional Materials* **34**, 2309335 (2024).